Using optical resonances to control heat generation and propagation in silicon nanostructures

Stefano Danesi,[a,b] *Ivano Alessandri*[a,c,d*]

[a] INSTM-UdR Brescia, via Branze 38, 25123 Brescia, Italy

[b] Department of Mechanical and Industrial Engineering, via Branze 38, 25123 Brescia, Italy

[c] Department of Information Engineering, University of Brescia, via Branze 38, 25123 Brescia, Italy

[d] INO-CNR, via Branze 38, 25123 Brescia, Italy

Supplementary Material

S1. Details of the model

S2. Optical resonances in Si-NPs

S3. Time intervals utilized for sampling in time-dependent simulations

S4. Extended study on substrate dependence

S5. Extended study on AR dependence

S6. UV light irradiation and the role of optical resonances

S7. Dependence of refractive index on temperature

S8. Modulated laser power

References

S1. Details of the model

With reference to the Nakamura equation described in the **Methods** section, further details are here reported about the crystallization kinetics modelling. The isothermal constant k has been related by the Johnson-Mehl-Avrami-Kolmogorov (JMAK) model to the nucleation and growth rate (N and G respectively) through the following expression:

$$k = \frac{\pi}{3} N \cdot G^3 \quad (1)$$

Both nucleation and growth rate depend on time, grain size and temperature. The grain size dependence of the nucleation rate reflects the probability of having nuclei with different radii as a result of the stochastic nature of nucleation process. The time dependence of the nucleation rate reflects the lower probability of nucleating a critical seed when the growth of the other seeds has been extended over part of the available amorphous volume. The dependence of growth rate on the grain size and time reflects the "double growth" kinetics, which is typical of silicon. The second kinetics is responsible for the explosive growth observed in the mid-advanced stages of crystallization, usually when the 20-40% of the volume has already been crystallized. All the detailed analytical expressions were reported by Spinella *et al.* (1). As a consequence, the isothermal JMAK constant k is time-dependent. Its behavior can be summarized as follows: At the early stages of nucleation k is constant, until Xc reaches a value about 0.4. In the second step, it rises as a consequence of explosive growth. In the latter case, volume effects become predominant. This picture is particularly adequate when processing temperatures are smaller than 900 °C. Olson and Roth (2) experimentally find the value of k at the first stage of crystallization for temperature spanning from 500 °C to 1000 °C. The expression they obtained is:

$$k(T) = k_0(T) \cdot e^{-\frac{E_a}{k_B \cdot T(r)}} \quad (2)$$

where $k_0 = 2.5 \cdot 10^{17} \left[\frac{1}{s}\right]$ and is temperature independent, E_a the activation energy (3.96 eV), k_B is the Boltzmann constant, and $T(r)$ is the absolute temperature. The dependence of k on the pillar radius and boundary effects has not been accounted in this model (3).

Materials modeling

The values describing the thermal and optical proprieties of the materials, depend by the value of Xc and temperature. Xc results from the solution of Nakamura equation, while temperature is extracted from Fourier equation of heat diffusion. In the following we detail the dependence of the thermal and optical parameters by T and Xc. The materials used in this work are c-Si, a-Si, Au, SiO_2. Except for the thermal conductivity of c-Si, no size dependence has been assumed for the other materials parameters. The non-linearity nature of the equations involved in the model, makes not possible to find analytical solutions.

The three thermal parameters required to solve the time dependent heat diffusion equation, are density ρ, the heat capacity at constant pressure C_p and the thermal conductivity k. The density of silicon was defined as a linear function of Xc :

$$\rho\,(T,Xc) = \rho_{a-Si}(T) \cdot (1 - X_c) + \rho_{c-Si}(T) \cdot X_c \quad (3)$$

where $\rho_{a-Si}(T)$ and $\rho_{c-Si}(T)$ are the temperature dependent amorphous and crystalline silicon densities. The plots of temperature dependence of density for amorphous and crystalline silicon was taken from ref (4) and are reported in Figure S1 b and a. For gold (5) and SiO_2 substrates, the density was taken from ref. (6) and reported in Fig. S1 c and d, respectively.

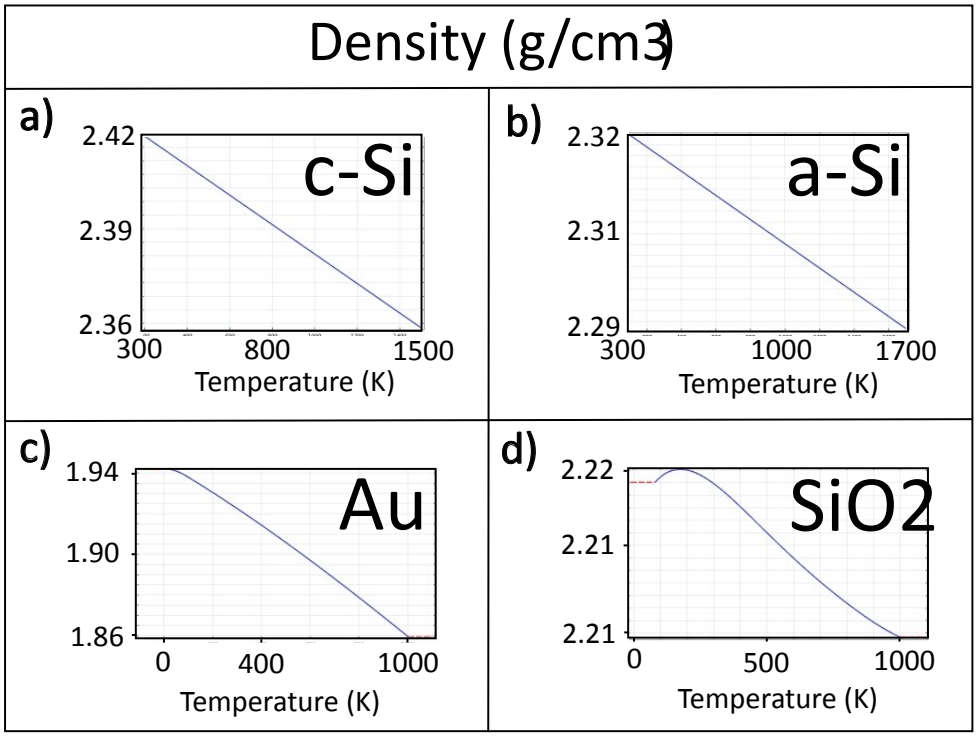

Figure S1 Temperature dependent density of amorphous and crystalline silicon (panels b and a); temperature dependent density of gold and silica (panels c and d). All the densities are here reported in g/cm^3.

The heat capacity of Silicon was defined as

$$C_p\,(T,Xc) = C_{pa-Si}(T)\cdot(1-X_c) + C_{pc-Si}(T)\cdot X_c \quad (4)$$

where $C_{pa-Si}(T)$ and $C_{pc-Si}(T)$ are the temperature dependent amorphous and crystalline heat capacities. The values of $C_{pc-Si}(T)$ and $C_{pa-Si}(T)$ was taken from ref. (7,8) and is reported in Figure S2 a and b. For gold and silica the heat capacity was taken from ref. (9,10) and are reported in Fig. S2 c and d.

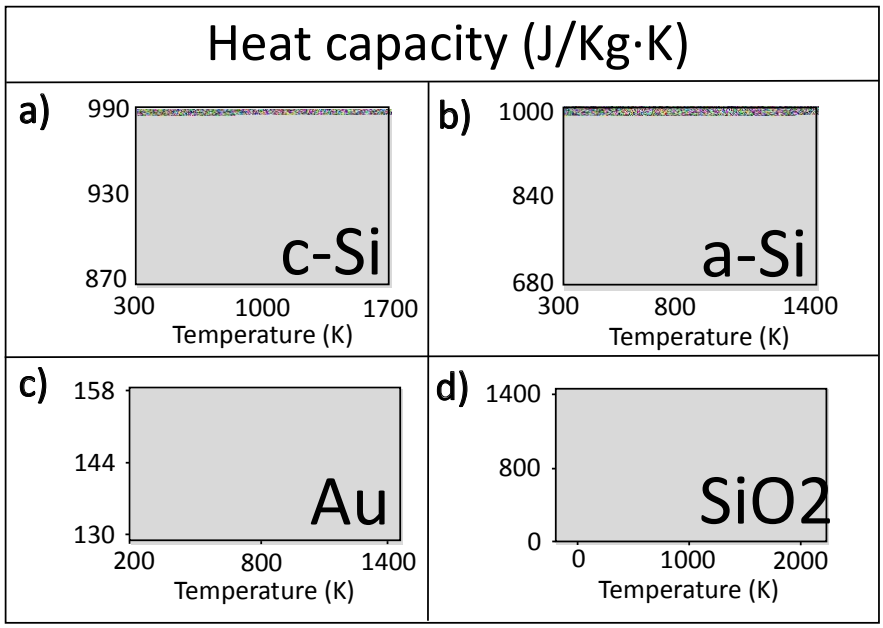

Figure S2 temperature dependent heat capacity of amorphous and crystalline silicon (panels b and a); temperature dependent heat capacity of Gold and Silica (panels c and d). All the quantities are reported in J/(Kg $\cdot K$).

The thermal conductivity used for Silicon is

$$k(T,Xc) = k_{a-Si}(T) \cdot (1 - X_c) + k_{c-Si}(T) \cdot X_c \quad (5)$$

The a-Si thermal conductivity k_{a-Si} was set at the constant value equal to 1.5 $W/m \cdot K$ (11-13). Its value can be considered independent by temperature and size. The thermal conductivity of c-Si, instead, strongly depends by temperature and size. For the reference system considered in this work (pillars with aspect ratio much larger than 1), the critical size is represented by the diameter, indicated with the term h. Considering the bulk temperature dependence (14-16) $k_T(T)$ and the thermal conductivity accumulation function (17,18) $\alpha_{\%}(h)$ for the size dependence, $k_{c-Si}(T,h)$ can be expressed as:

$$k_{c-Si}(T,h) = k_T(T) \times \alpha_{\%}(h) \quad (6)$$

The accumulation function is defined as the ratio between the thermal conductivity value computed for a film of thickness h and the bulk value. $\alpha_{\%}(h)$ gives the contribution to the thermal conductivity provided by phonons with mean free path up to h. $k_T(T)$ is the bulk thermal conductivity of c-Si,

whose dependence by temperature is reported in figure S3 a. For gold and silica the thermal conductivity was taken from ref. (19, 20) and are reported in fig. S3 b and c.

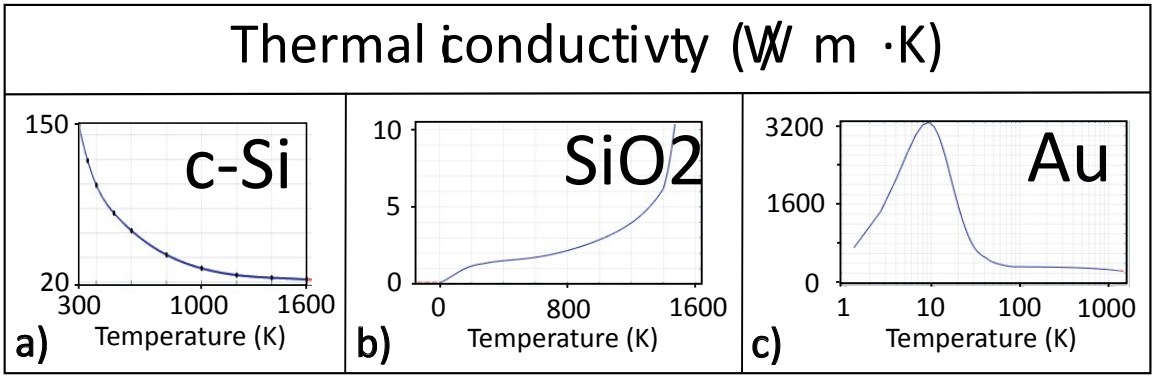

Figure S3 Temperature dependent thermal conductivity of crystalline silicon (panel a), Silica (panel b) and gold (panel c). All the quantities are reported in W/(m $\cdot K$).

For bulk c-Si at room temperature k_{c-Si} assume the value of 150 $W/m \cdot K$. For nanostructures of diameter of 10 nm and temperature higher than 700 K, k_{c-Si} is lower than 1 $W/m \cdot K$.

The two parameters required to solve Maxwell equations are the real and imaginary part of dielectric constants. The values of the dielectric constants used in this work for Silicon are

$$\varepsilon' = \varepsilon_{a-Si}'(1 - X_c) + \varepsilon_{c-Si}' X_c \quad (7)$$

$$\varepsilon'' = \varepsilon_{a-Si}''(1 - X_c) + \varepsilon_{c-Si}'' X_c \quad (8)$$

where $\varepsilon_{a-Si}'(\lambda = 532\ nm) = 18.830$, $\varepsilon_{c-Si}'(\lambda = 532\ nm) = 17.237$, $\varepsilon_{a-Si}''(\lambda = 532\ nm) = 7.770$ and $\varepsilon_{c-Si}''(\lambda = 532\ nm) = 0.430$ (21,22). For gold (23) $\varepsilon_{Au}'(\lambda = 532\ nm) = -4.2857$, $\varepsilon_{Au}''(\lambda = 532\ nm) = 2.3317$, and for SiO_2 $\varepsilon_{SiO2}'(\lambda = 532\ nm) = 2.1$, $\varepsilon_{SiO2}''(\lambda = 532\ nm) = 0$ (24).

Boundary conditions

Boundary conditions was applied to the system in order to obtain a single solution. On all the air-exposed boundaries of our model, the convection boundary was applied:

$$q_c \cdot n = h_c(T_{ext} - T) \quad (9)$$

where q_c is the convective heat flux, n is a versor normal to the surface and h_c is the heat transfer coefficient, whose expressions was taken from references (25-30) for different geometries. T_{ext} is the external absolute equilibrium temperature fixed at the room temperature $293.15\ K$.

In order to account for the conduction contribution of air, an air domain surrounding all the exposed surfaces has been included in the model. The radiative thermal dissipation contribution has been considered by imposing Stefan-Boltzmann equation on all the air exposed surface.

$$q_r \cdot n = A\ \sigma\ \varepsilon\left(T^4 - T_{ext}^4\right) \quad (10)$$

where q_r is the radiative heat flux, A the area of the exposed surface, σ is the Stefan-Boltzmann constant, ε the surface emissivity. For a-Si $\varepsilon_{a-Si} = 0.9$, for c-Si $\varepsilon_{c-Si} = 0.7$ and for SiO_2 $\varepsilon_{SiO_2} = 0.8$. The surface emissivity on the pillar boundaries was defined by the following approximation $\varepsilon = \varepsilon_{a-Si} \cdot (1 - X_c) + \varepsilon_{c-Si} \cdot X_c$.

At the boundary between two thermally different materials, a Kapitza resistance has been defined. The value at the amorphous-crystalline Silicon interface was set at

$$R_K^{a/c-Si} = -1.25 \cdot 10^{-12} \cdot T + 0.75 \cdot 10^{-9} \left[\frac{K \cdot m^2}{W}\right] \quad (11)$$

while at the a-Si/SiO_2 and c-Si/SiO_2 interface was set at $R_K^{Si-SiO_2} = 1 \cdot 10^{-9}\ m^2K/W$ (31,32).

The Air domain surrounding the nanostructure and the Solid domain sustaining the nanostructure was modeled as 10 μm edge cubes. On the faces of these cubes, the temperature was fixed, equals to the reference value at room temperature, 293 K. With a parametric modulation of the edge length we ensure that the temperature satisfy a convergence condition at 10 μm. This check ensures that, for the system under investigation and within the temperature ranges spanned in this work, the

volume of 1000 μm^3 for the substrate and air is sufficiently large to replicate the effect of an infinitely large equivalent volume. From a computational viewpoint, this assumption considerably reduces the computational burden, which made possible to run Finite Element Analysis without cluster computing.

The localization of temperature

The local and selective crystallization of silicon is possible because the material sustains large temperature gradients. In general, this is possible when thermal conductivity is sufficiently low. Amorphous Silicon can be synthesized in order to have very low thermal conductivity. In Figure S4 is reported the profile of the maximum temperature along the pillar axis, for different times during processing. The inset shows the temperature map in color scale, obtained by solving heat diffusion equation before crystallization. The lines show the time and spatial evolution of temperature profile.

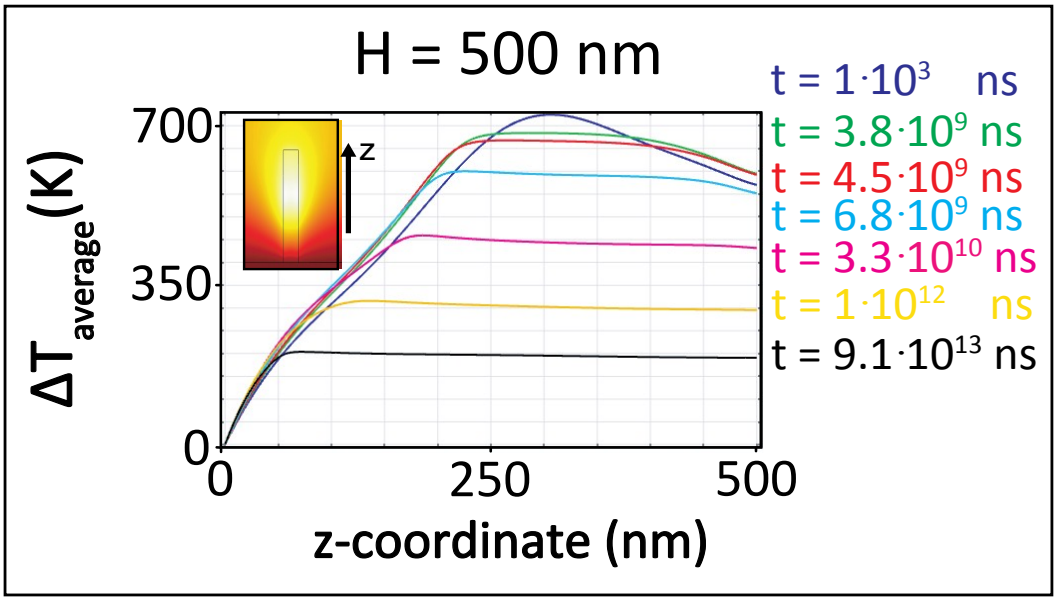

Figure S4 Temperature profile along the pillar axis, taken at different times during a crystallization process. The exciting wavelength is 532 nm, the pillar height is 500 nm and the diameter is 80 nm.

We can clearly observe a strong temperature gradient before the crystallization between the central region and the tip. This gradient is responsible for the different kinetics of crystallization in the different regions of the pillar. According to temperature distribution, the central region will

crystallize first. After that, the profile changes and the gradient in the crystallized portion decreases until it disappears completely. This can be attributed to the larger thermal conductivity of polycrystalline silicon respect to amorphous silicon.

Heat dissipation mechanisms: conduction, convection, radiation.

Figure S5 shows the different components that control heat dissipation in the pillar.

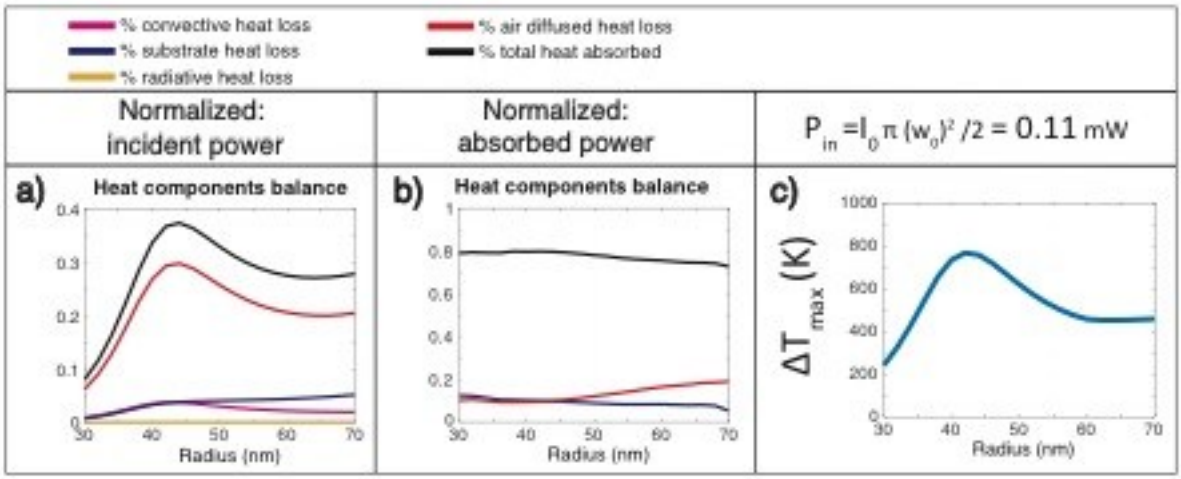

Figure S5 Contribution of different factors that control heat dissipation in a-Si pillars.

The curve in violet shows the amount of convective heat dissipated through lateral walls, the blue one shows the heat flowing through the basis of the pillar, the yellow one the radiative heat and the red one the heat diffused in air. The black curve shows the total power absorbed by the pillar and the dashed green line shows the sum of all the components. The height of the pillar was set at 500 nm, and the radius was spanned from 30 nm to 70 nm, corresponding to aspect ratios in the range 8.3 to 3.5, respectively. In panel a, heat is normalized to the incident power, whereas in panel b it has been normalized to the absorbed power. Panel c shows the maximum temperature shift in comparison to room temperature inside the pillar.

From these data we realize that thermal radiation is negligible, in comparison to the total absorbed power. On the other side, heat flowing into the substrate is between the 10% and 20% of the total heat absorbed (red line panel b) depending on the value of the radius. In particular, it increases for radii > 50 nm. This is reasonable, because the larger contact area facilitates the heat flow through the substrate. On the other hand, for small sizes, the reduced contact area behaves as a bottleneck, preventing the efficient heat diffusion through the substrate, even in the case of substrates with high thermal conductivity.

If we artificially set the substrate thermal conductivity 5 times lower and 5 times higher than that of

c-Si, we obtain the results shown in figure S6 and S7, respectively. The temperature (panel c) is basically unaltered: no differences are observed between the two different cases. These results suggest that the crystallization kinetics and heat components (panels a and b) will not significantly change as well.

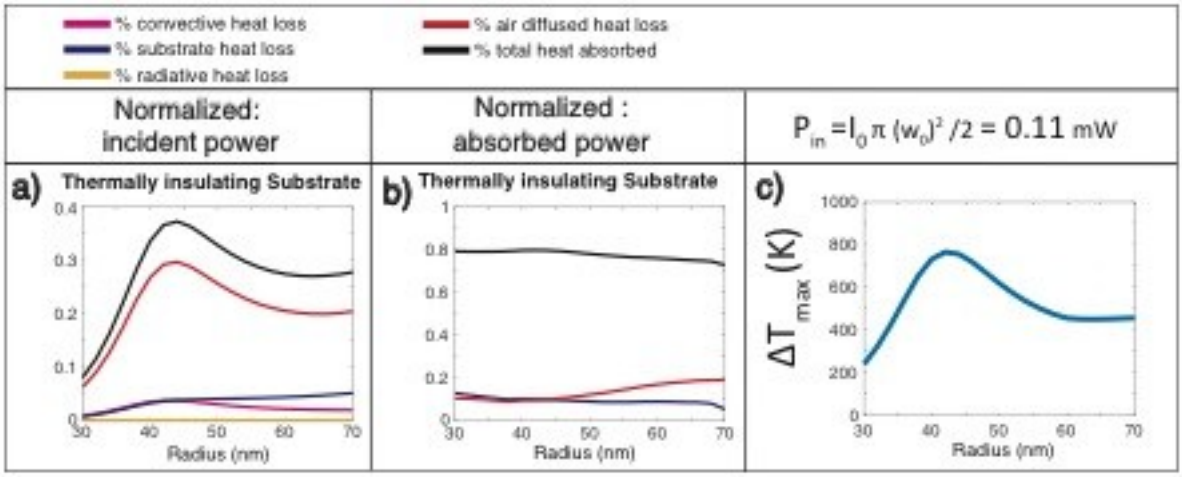

Figure S6 Simulations of different contributions to heat dissipation for a-Si pillars in contact with thermally insulating substrates (thermal conductivity 5 times lower than that of c-Si substrates).

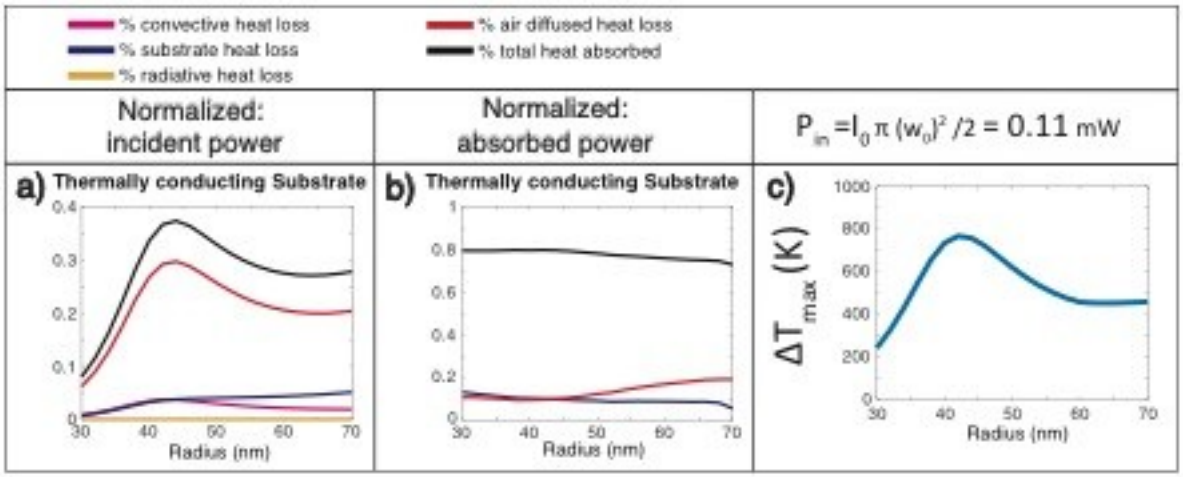

Figure S7 Simulations of different contributions to heat dissipation for a-Si pillars in contact with thermally conducting substrates (thermal conductivity 5 times higher than that of c-Si substrates).

A second factor to be taken into account in discussing about the role of the substrate in mediating heat transfer is that heat is not generated homogeneously in the pillar but is concentrated in specific regions (in particular in the middle for most of the pillars investigated in the present work As pillars are made of amorphous Si, which is low conducting material (k=1 W/(m*K)), heat is easily dissipates in air by conduction and convection. As a consequence of energy localization, large temperature gradients are generated, which can be used for texturing the system.

Thus, under these conditions the substrate is not significantly influencing the thermal properties of the pillar. On the other hand, as the substrate can strongly influence the far-field light absorption

capability of the pillars, it is expected to play a role in determining the temperature of the system. As heat dissipated through the lateral walls of the pillar dominates the heat loss mechanisms, a proper discussion on the choice of convective heat transfer coefficient is needed. Convective heat transfer coefficient for the vertical cylinder was set equal to:

$$h = \frac{k}{H}\left(\frac{4}{3}\left(\frac{7 \cdot Ra_H \cdot Pr}{5(20 + 21 \cdot Pr)}\right)^{1/4} + \frac{4 \cdot (272 + 315 \cdot Pr) \cdot H}{35 \cdot (64 + 63 \cdot Pr) \cdot D}\right) \qquad (12)$$

where D is the cylinder diameter, H is the cylinder height, Pr is the Prandtl number, given by:

$$Pr = \mu \cdot \frac{C_p}{k} \qquad (13)$$

μ ,C_p and k indicate dynamic viscosity (Pa·s), heat capacity at constant pressure (J/(kg·K)) and thermal conductivity (W/(m·K)), respectively. R_{aH} is given by:

$$Ra_H = \frac{g \cdot \alpha_p \cdot |T - T_{ext}| \cdot H^3}{k \cdot \mu} \qquad (14)$$

where g is the acceleration of gravity (m/s^2) and T_{ext} was set to the value of room temperature. This expression was taken from ref. 34.

Fig. S8 shows the temperature dependence of convective heat transfer coefficient for two different pillar radii and heights.

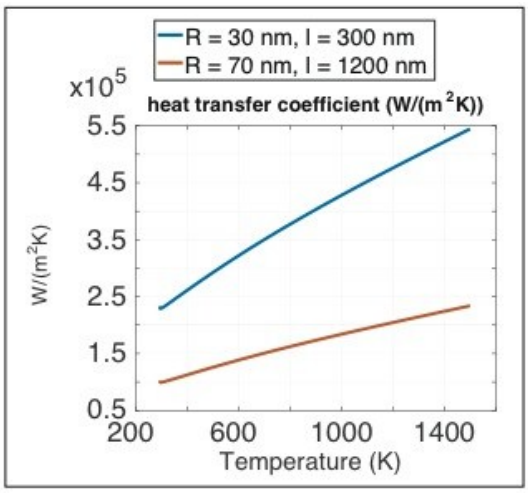

Figure S8 Temperature dependence of convective heat transfer coefficient for pillars with two different radii and heights.

When the geometrical features are at the nanoscale, however, a decrease in the value of h can be observed (*see* ref. 37). To the best of our knowledge, no studies have been performed on vertical nanopillar geometries, so we decide to analyse two limit cases:

1) The convective heat transfer coefficient is null.

2) The convective heat transfer coefficient is that obtained from equation (12) (Fig. S5).

Fig. S9 shows the heat loss components for h=0. Values are normalized respectively to the incident power (panel a) and to the absorbed power (panel b). Finally, panel c displays the maximum temperature shift with reference to the room equilibrium temperature.

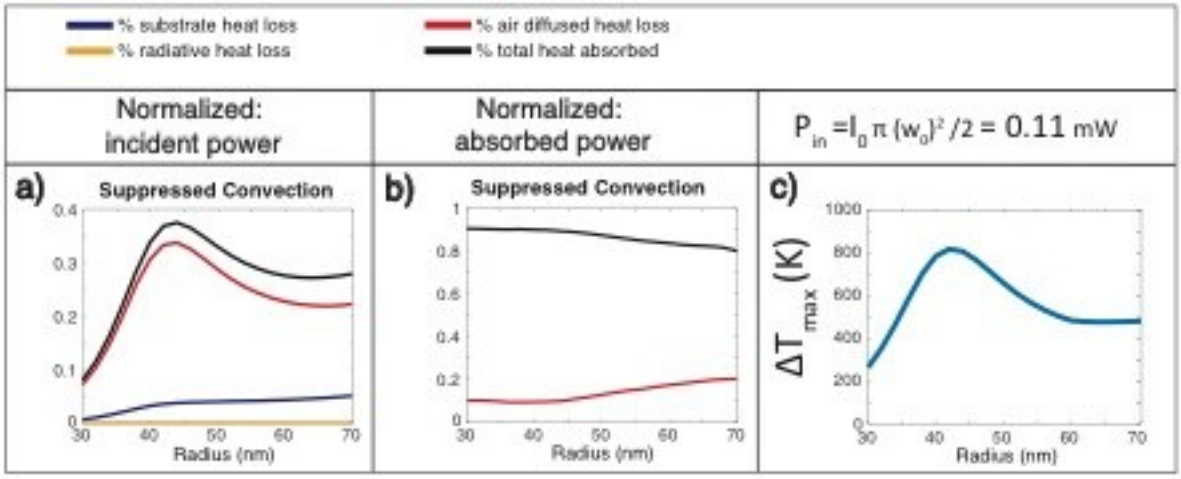

Figure S9 Heat dissipation components for h=0.

Heat dissipated through the substrate is not significantly modified, while heat dissipated by air conduction increases by a factor that is equal to the convective heat loss. This becomes evident by comparing panels a and b of fig. R5 with panels a and b of fig. S5. Even the maximum temperature enhancement is very close. The maximum difference between the two temperatures is observed at 42.5 nm, and is equal to 50K. In figure R6 is reported the value of X_c average kinetics for a pillar with radius 42.5 nm and height 500 nm in the two cases: with h=0 and h equal to eq. (12). The real crystallization kinetics is expected to lay between those two limiting cases (Fig. S10).

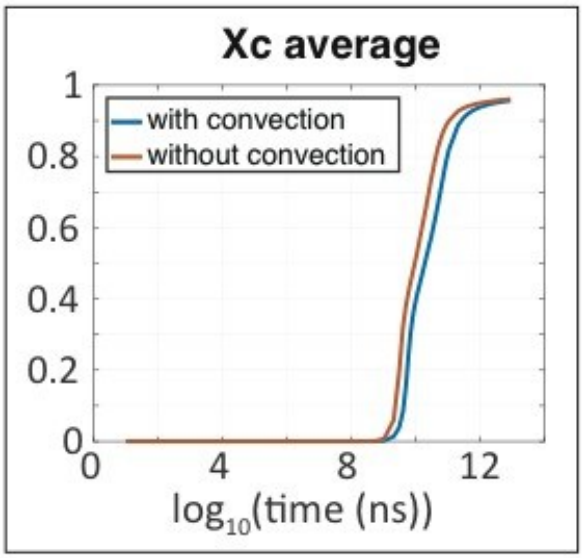

Figure S10 Crystallization kinetics in a pillar of height 500 nm and radius 42.5 nm, exposed to a CW laser of 0.11 mW power and 0.9 N.A. The two curves represent the values obtained by setting the convective heat transfer coefficient equal to zero (orange curve) and equal to equation (12) (blue curve).

We decided to consider the less favourable situation, in which the kinetics is slower. This case corresponds to the situation where the thermal convective coefficient assumes the value reported in (12).

Validity of Fourier's Law

It is well known that for nanostructures, even if the characteristic length is much larger than the mean free path of heat carriers, corrections to Fourier low should need to be accounted. (35) In this case the continuum assumption is still valid but heat conduction equations must be reviewed with the thermomass and phonon hydrodynamic theory, which account for the inertial origin of heat energy. (36) This heat propagation regime is usually called Non-Fourier conduction (NFC)

The criteria to be satisfied for NFC is that the characteristic length of the structure D is comparable (equal to or lower) to the characteristic length for NFC, l:

$$D = \frac{2ab}{a+b} \quad (14, ref.37)$$

$$l = \frac{q \cdot k}{2 \cdot \alpha \cdot C \cdot (\rho \cdot C \cdot T)^2} \quad (15, ref.38)$$

where a and b are respectively the pillar diameter and height, q is the heat flux (W/m^2), k the thermal conductivity (W/(m·K)), α is a proportional parameter, which for silicon is equal to 1, C is

the specific heat of solid (J/K), ρ is the density (kg/m^3) and T is the temperature (K).

For a pillar of 500 nm height and 85 nm diameter, D is equal to 145 nm. Panel b of figure S11shows the heat flux modulus in the pillar. The larger values are focalized to the pillar basis. Because heat flux is not homogeneous we consider the maximum value, which is 9·108 W/m^2. Panel a of fig. S11 shows the value of l for a-Si and c-Si for temperatures ranging from 1 K to 1200 K.

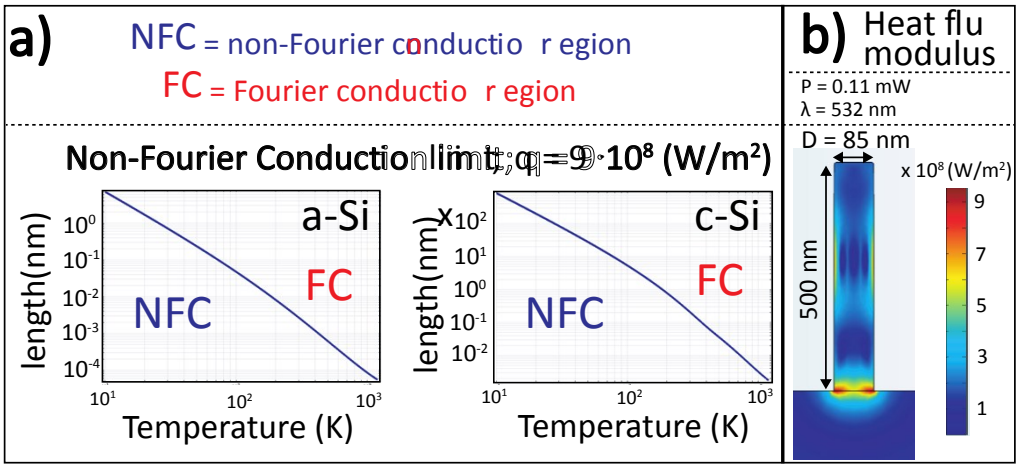

Figure S11 Non-Fourier vs. Fourier regime. Panel a shows the limit between the NFC regime and the FC regime for a-Si and c-Si. The two curves have been calculated considering the heat flux fixed at 9·10^8 W/m^2. Panel b: heat flux modulus in the pillar.

In the case of a-Si, except for cryogenic temperature, the value of l is always lower than the atomic radius, and no non-Fourier conduction can be observed. In the case of c-Si, the characteristic length is much larger, mainly because of the larger thermal conductivity of c-Si respect to a-Si. We can conclude that heat fluxes, temperatures and sizes involved in our work allowed the use of Fourier law corrections to be avoided for both for a-Si and c-Si.

Analysis of stress and strain evolution

Laser-induced crystallization introduces strain and stress into the pillars, as shown in Fig. S12.

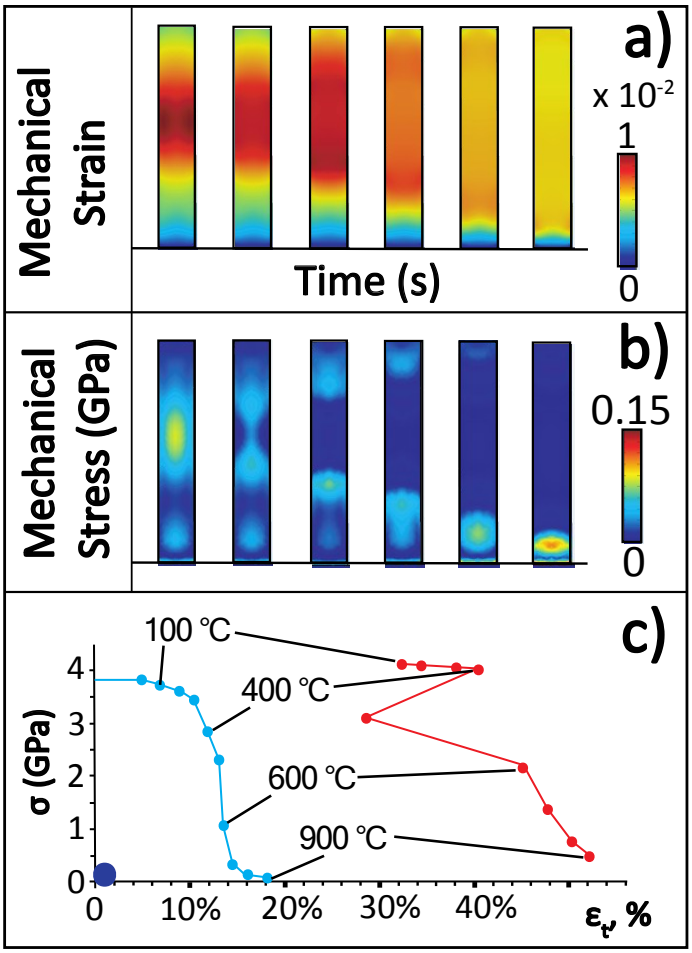

Figure S12 Panel a displays the volumetric mechanical strain, panel b the absolute value of mechanical stress, in GPa, and panel c the strain-stress curves for c-Si as a function of different temperatures, which ranges from room temperature to 900 °C. Data for figure in panel c were taken from ref. 39. The time intervals in panels a and b are 0.001 s, 3.1 s, 6.1 s, 11 s, 31 s, 81 s, respectively.

Stress originates from the thermal expansion of materials and different density between amorphous and crystalline phase. The maps in fig. S12 show how tension and strain moduli are spatially distributed.

The strain reaches its maximum for a value that is 1% of the volume, so we can neglect the deformation thermal deformation of the geometry. The maximum deformation is located in the hotspot. The stress is initially located in the middle of the structure. As crystallization takes place, the stress propagates to the interface between the crystalline and amorphous region. The maximum stress and strain observed in the structure during processing are respectively 1% and 0.15 GPa, respectively. Those coordinates in the σ-ε plane correspond to the blue spot highlighted in panel c of fig. S12. The value, near the origin, lies in the elastic deformation regime, and is far from the inelastic deformation regime and breaking point. For this reason, we do not expect that irreversible

deformations of the pillar geometry would take place at the processing temperatures used in the present work.

Another problem is the deformation coming from the long duration of the processing. Keeping the pillar at high temperatures for such a long time (> 24h), in fact, can modify the geometry irreversibly. This is very common for melt-mediated crystallization because the liquid phase is subjected to reshaping. In the solid-phase-crystallization it is much less common, but it cannot be ruled out *a-priori*.

S2. Optical resonances in Si-NPs

Figure S13 show the comparison between heating and absorbed power for two different exciting wavelengths. The first row, refers to the laser processing at wavelength 266 nm, the second at wavelength 532 nm. The pillar has an AR of 6.25, a diameter of 80 nm and is 500 nm height. This geometry is close to the visible resonance and is far respect to the 266 nm resonance. Panels b and e show the absorbed power in the two different exciting conditions.

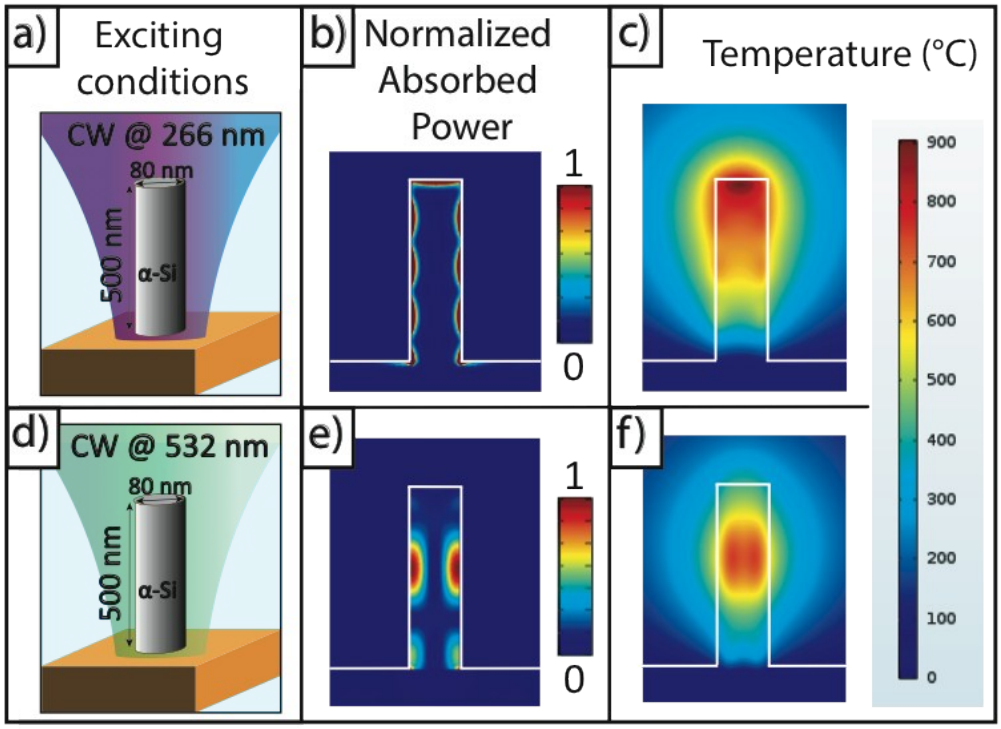

Figure S13 Role of optical resonances in the excitation of silicon nanopillars. Normalized absorbed power (panels (b) and (e)) and absolute temperature (panels (c) and (f)) in silicon pillars excited in different conditions. Panels (a) and (b) schematically report the exciting conditions and the geometrical features of the pillars. The substrate in this case is crystalline silicon.

Under UV irradiation, the power is deposited on the top and on the lateral walls of the pillar. The penetration depth of the radiation however is very small, in fact, only the skin of the pillar in interested by optical absorption. At visible wavelength, instead, radiation efficiently couple to the resonant mode at 532 nm, which penetrate much more in the pillar. The power is then deposited only in a specific region, and can easily reach the points inside the structure. The different absorption pictures result from very different thermal response (Figure S13, c and f). In the UV, temperature is localized at the top, while in the visible temperature localize at the center. This temperature inhomogeneity determines different crystallization kinetics in different regions of the pillar.

S3. Time intervals utilized for sampling in time-dependent simulations

In this section are reported the sampling times of the Figures 1 and 4 of the main text.

Figure 1	**Sampling time (s)**
a	0, 2400, 4800, 7200, 9600, 12000, 14400
b	0, 0.2, 0.4, 1, 4.2, 200, 91400
c	0.004, 3.8, 4.5, 6.7, 33, 960, 91400
d	0, 2.1, 3.1, 5.1, 41, 91400
e	0, 7.1, 11, 21,31,91400
f	0, 9.9, 71, 91, 110, 91400
g	0, 11, 21, 41, 71, 91400
i	0, 0.9, 3.2, 21, 81, 91400
l	0, 51, 81, 90, 210, 91400
m	0, 7.2, 31, 306, 3060, 91400

Figure 4	Sampling time (s)
c, d	0.004, 3.8, 4.5, 6.8, 33, 1000, 91400
e, f	0.004, 3.8, 4.5, 6.8, 33, 1000, 91400

S4. Extended study on substrate dependence

Figure S14 shows the temporal evolution of crystallization as a function of different substrate material. The materials are gold, silicon and SiO_2, representative of conductors, semiconductors and insulating materials, respectively. The reference case of a free-standing pillar is also reported (panel d and h). The pillars have an AR of 4.4 and 13.3, and height of 400 nm and 1200 nm, respectively. The radius is 45 nm for both the pillars.

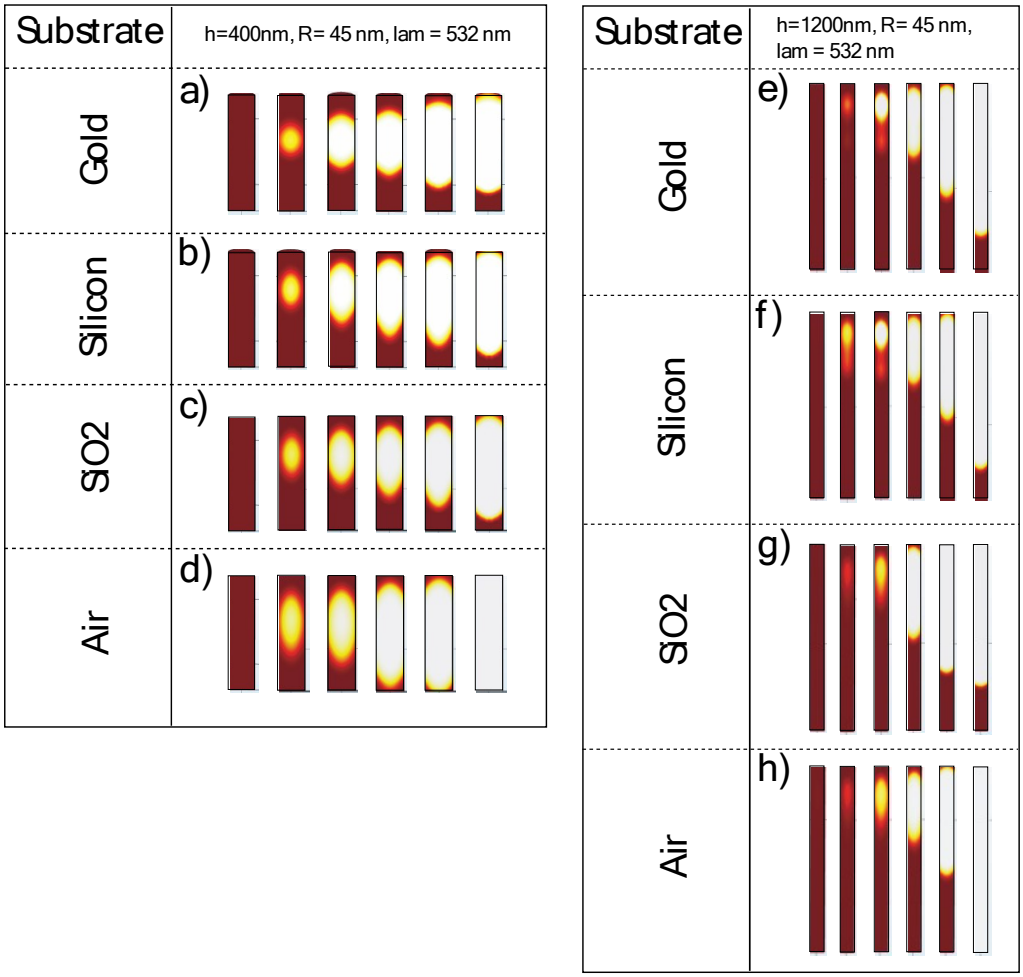

Figure S14 Time evolution of the crystallization for different substrates materials and for different aspect ratios: 4.4 and 13.3 respectively. The initial and final time are respectively 0 s and 25.4 h.

Figure S6	Sampling time (s)
a	0, 21, 31, 51, 11000, 91400
b	0, 21, 31, 51, 110, 91400
c	0, 41, 51, 61, 81, 91400
d	0, 31, 41, 51, 71, 91400
e	0, 0.81, 1.1, 2.1, 6.1, 91400
f	0, 2.1, 3.1, 6.1, 9100, 91400
g	0, 9.2, 11, 21, 210, 91400
h	0, 3.2, 5.2, 7.2, 21, 91400

When the resonance is localized in the top of the pillar, the effect of the substrate material tends to be negligible. This can be reasonably attributed to the lower influence of the changed optical environment. In the case of 1200 nm height pillar (panels e-h) the position of the crystalline hotspot remain unchanged for the different substrates, even if the evolution picture seem to be slightly different in the case of Gold and Silicon respect to the case of Air and SiO_2. Small modifications concerning the position of the crystalline hotspot can be observed for the 400 nm height pillars (panels a-d). In pillars of height 300 nm (Fig. 1 of the main text) the position of the hotspot is much more affected by the substrate. This has already been argued in the main text section 3.

S5. Extended study on AR dependence

The study of contemporary crystallization of multiple spot in the pillar has been extended to pillars with height 640 nm. The result is shown in Fig. S15 a and b.

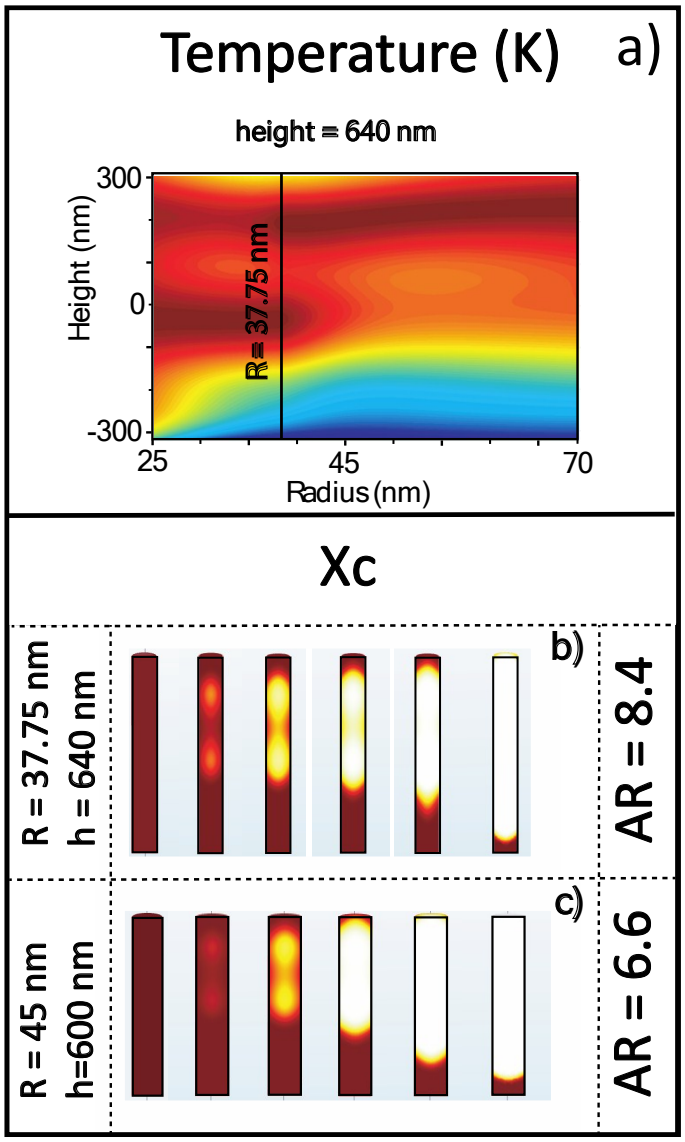

Figure S15 Panel a plot the temperature distribution along the pillar as a function of the radius, for a pillar with height 640 nm. In panel b-d are reported the crystalline field Xc at different times for the two combination radius 37.75 nm, height 640 nm, and for radius 45 nm, height 600 nm.

Figure S15	Sampling time (s)
b	0, 17, 21, 26, 78, 91400
c	0, 51, 81, 91, 210, 91400

In panel a is shown the temperature value along the pillar, for radii varying from 25 nm (AR=12.8) to 70 nm (AR=4.5). In panel b is shown the evolution of the crystalline field Xc at different times for a pillar with radius 37.75 nm, and AR = 8.4. This pillar shows two peaks of temperature at

different positions of the pillar. Panel c of Fig. S15 refers to a pillar of radius 45 nm and height 600 nm. In this case the system has two peaks of temperature which are closer. The larger spacing of the temperature peaks enable enables a better resolution between the two crystallized hotspots.

In conclusion we show that by properly design the resonances in a nanostructure we can finely tune the distance between crystallization hotspots.

S6. UV light irradiation and role of the optical resonances

In this section we report the optical proprieties of a pillar processed with an UV radiation. In fig. S16 is reported the absorption and scattering cross section as a function of time, referred to the crystallization with UV radiation (266 nm) described in figure 1 b of the main text. The pillar has an AR of 6.25 with a height of 500 nm and is supported on a c-Si substrate.

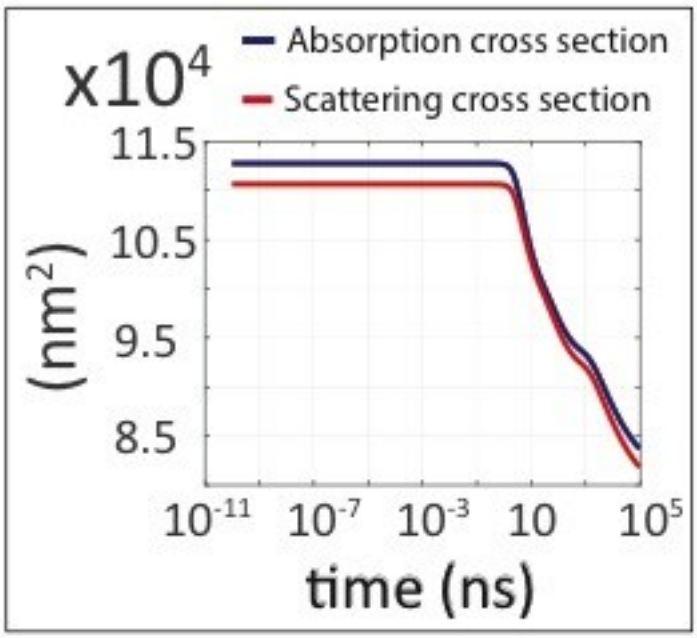

Figure S16. Temporal evolution of the absolute absorption and scattering cross sections during the crystallization. The processed system is a pillar with height 500 nm and AR 6.25.

In the UV processing the system is out-of-resonance and the optical proprieties are not enhanced. The enhancement of the optical properties under Vis irradiation is further investigated. In order to have a deeper understanding on the role of resonances in visible light processing, we studied the

temporal evolution of photon absorption, for a larger range of diameters. We considered Si-P with AR spanning from 6.1 to 2.6 (radii ranging from 30 nm to 70 nm), and keeping the height constant at 368 nm. The total power absorbed by the pillar was divided in two components: the power absorbed by the amorphous phase and the power absorbed by the polycrystalline phase, using the same method explained in the main text. Results are shown in Fig. S17.

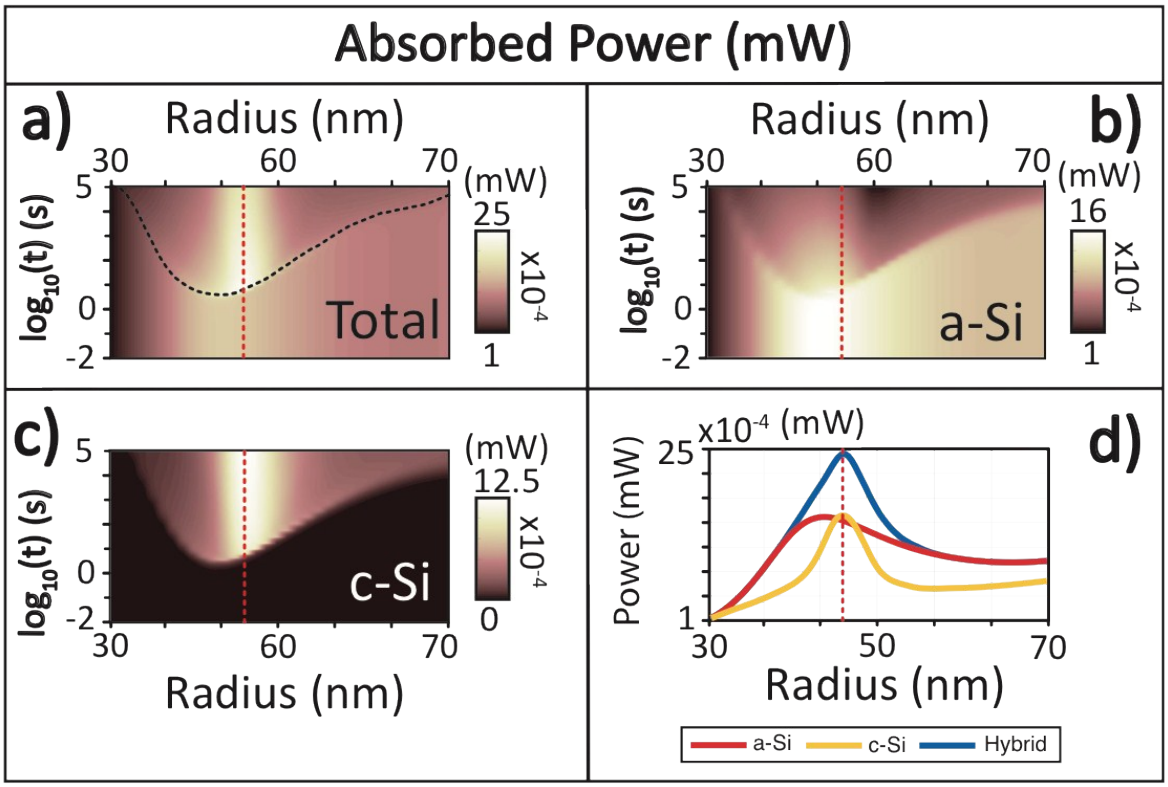

Figure S17 Absorbed power in mW of silicon pillars with fixed length (368 nm) and radius spanning from 30 to 70 nm. Panel a show the total absorbed power, panel b and c show the portion absorbed by amorphous and crystalline components of the pillars during their laser processing. Panel d show respectively the power absorbed before the processing (red line), after the complete processing (yellow line), and the maximum absorption during the processing (blue line). Dashed black line, in panel a, show the position at which such maximum is observed. The red dashed line shows the position of sample B in the range of radii considered in this study.

Figure S17.d show the total absorbed power before crystallization (red line), after complete crystallization (yellow line) and the maximum value obtained during crystallization (blue line). Before processing, the highest absorption is achieved when the radius is 42.5 nm while after complete processing, the maximum absorption is achieved when the radius is 45 nm. When the absorbed power is maximum (blue line) the system is not completely crystallized. Its peak is

located at the resonance of the c-Si pillar. This result suggests that the optimal performances in the enhanced absorption regime take place when the amorphous pillar has the geometric features of the crystalline pillar, which is in resonance with the exciting radiation. This can represent a criterion for engineering hybrid resonant structures with enhanced absorbing performances and will be further investigated in forthcoming studies.

S7. Dependence of refractive index on temperature

In the previous results, the temperature dependence of the optical refractive index of c-Si was neglected. The reason behind this choice was that this kind of dependence considerably slows down the convergence of a solution for a Finite Element solver due to the addition of nonlinearity in the systems of equations involved in the problem solution. Indicatively, for a pillar with AR 6.25, height 500 nm and diameter 80 nm, we optimize a computation time of 10 hours. By including the temperature dependence, the same system is solved in 48 hours.

For those reasons we analyze the role of temperature dependence for a single nanopillar and compare the results with the temperature independent case. The expression of n and k has been modified according to the relations obtained by (33)

$$n = n_0 + 4.5 \cdot 10^{-4}[K^{-1}] \cdot T[K]$$

$$k = k_0 + 0.1 \cdot 10^{-4}[K^{-1}] \cdot T[K]$$

In figure S18 are reported the maximum temperature (panel a), the absorbed power (panel b), the average crystallinity (panel c), and the absorption cross section (panel d) considering or not the temperature dependence of refractive index.

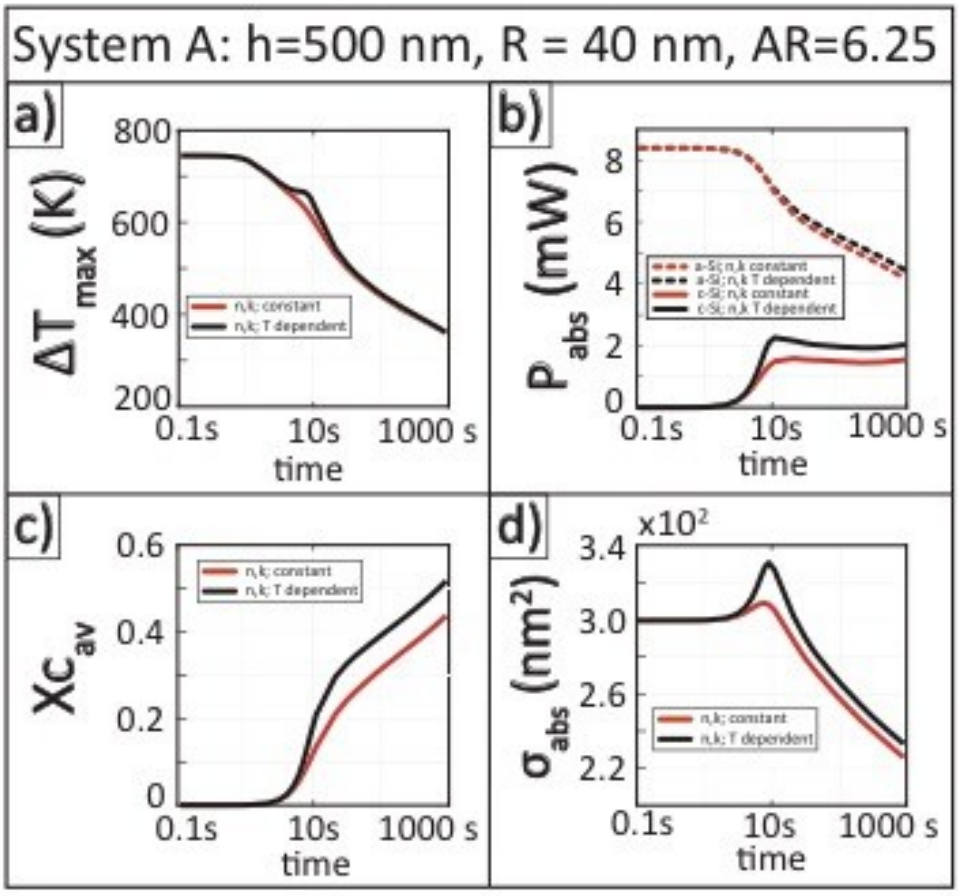

Figure S18 Comparison between the time evolution of the system, considering the temperature dependence of the complex refractive index (black line) and neglecting it (red line). The four panel show the temperature (a), the average crystallinity $X_{c,av}$ (c), the absorbed power (b) and absorption cross section (d).

The nonlinear refractive index, is responsible for a faster kinetics (panel c), and larger absorbed power and absorption cross section enhancement (panel b and d). It reinforces the hypothesis of the enhanced optical proprieties in the hybrid crystalline state, showing a more intense peak respect to the temperature independent counterpart. We can conclude that the analysis considering n and k independent by T gives results that are in good qualitative agreement with those obtained by taking this dependence into account. This approximate approach can be useful to obtain a fast preliminary prediction of the evolution of the crystallization dynamics, with major advantages in view of materials and process design. Once the parameters of interest have been pre-screened, more

accurate numerical results can be obtained for the selected systems by including the temperature dependence of the refractive index.

S8. Modulated laser power

A possible strategy to accelerate the crystallization kinetics without producing significant reshaping effects might be based on the modulation of the exciting power at different time intervals. For example, the exciting power could be doubled after the onset of partial crystallization, when temperature has reached 500 K. Panel b of Fig. S19 shows the comparison between the kinetic of the constant power *vs.* double power process.

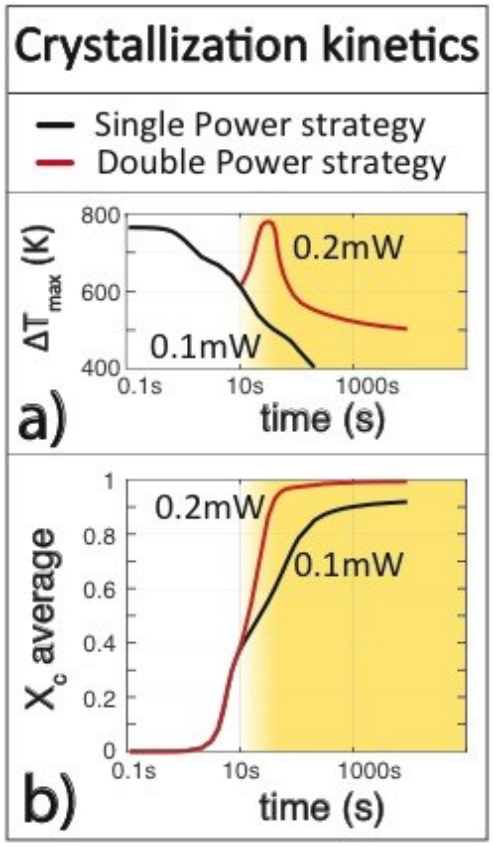

Figure S19 Comparison between the maximum temperature enhancement (panel a) and Xc average (panel b), obtained by using either single (black line) or double (red line) power excitation.

In the case reported in Fig. S19, the power was increased from 0.1 mW to 0.2 mW through a nonlinear ramp from 10 to 20 s. After 20 s the exciting power was maintained constant at 0.2 mW. This strategy significantly enhances the kinetics of crystallization. At 30 s, the 96% of the pillar is crystallized. The enhancement is due to an increase of the temperature (panel a).

References

(1) Spinella, C.; Lombardo, S.; and Priolo, F. Crystal grain nucleation in amorphous silicon. *J. Appl. Phys.* **1998**, 84, 5383.

(2) Olson, G.L.; Roth, J.A. Kinetics of solid phase crystallization in amorphous silicon. *Mat. Sci. Rep.* **1988**, 3, 1-78.

(3) Cahn, J. W. The kinetics of grain boundary nucleated reactions. *Acta Metall.* **1956**, 4, 449-459.

(4) Swenson, C.A. Recommended values for the thermal expansivity of silicon from 0 to 1000K. *J. Phys. Chem. Ref. Data* **1983**, 12, 179.

(5) Brown, T. L.; Lemay Jr, E. *Chemistry: the central science,* **1985**, Prentice Hall Inc, Englewood, New Jersey.

(6) Haynes, W. M. *CRC Handbook of Chemistry and Physics 92nd ed.* **2011**, CRC Press, Boca Raton.

(7) Okhotin, A. S., Pushkarskii, A. S., and Gorbachev, V. V. *Thermophysical Properties of Semiconductors* **1972**, "Atom" Publ. House, Moscow.

(8) Desai, P.D. Thermodynamic proprieties of Iron and Silicon. *Phys. and Chem. Ref. Data* **1986**, 15, 967.

(9) Touloukian, Y.S.; Ho, C.Y. Thermal Radiative Proprieties: Metallic Elements and Alloys. *Thermophys. Propr. Mat.* **1972**, 7.

(10) Touloukian, Y.S.; DeWitt, D.P. *Thermal Radiative Proprieties: Nonmetallic Solids.* **1970**, *Vol. 8*, United States.

(11) Wada, H.; Kamijoh, T. Thermal conductivity of amorphous silicon. *Jap. J. Appl. Phys.* **1996**, 35, 648-650.

(12) Moon, S.; Hatano, M.; Lee, M.; Grigoropulos, C. P. Thermal conductivity of amorphous silicon thin films. *Int. J. Heat and Mass Transf.* **2002**, 45, 2439-2447.

(13) Cahill, D. G.; Katiyar, M.; and Abelson, J. R. Thermal conductivity of a-Si:H thin films. *Phys. Rev. B* **1994**, 50, 6077.

(14) Touloukian, Y. S.; Powell, R. W.; Ho, C. Y.; Klemens, P. G. *Thermophysical Properties of Matter – The TPRC Data Series. Vol. 2. Thermal Conductivity-Nonmetallic Solids* **1970**, New York.

(15) Thompson, J. C.; and Younglove, B. A. Thermal conductivity of silicon at low temperatures. *J. Phys. Chem. of Solids* **1961**, 20, 146-149.

(16) Glassbrenner, C. J.; Slack, G. A. Thermal conductivity of silicon and germanium from 3 K to Melting point. *Phys. Rev.* **1964**, 134, A1058.

(17) He, Y.; Savić, I.; Donadio, D.; Galli, G. Lattice Thermal Conductivity of Semiconducting Bulk Materials: Atomistic Simulations. *Phys. Chem. Chem. Phys.* **2012**, 14, 16209-16222.

(18) Melis, C.; Dettori, R.; Vandermeuled, S.; Colombo, L. Calculating Thermal Conductivity in a transient conduction regime: theory and implementation. *The Eur. Phys. J. B* **2014**, 87-96.

(19) Powell, R.W.; Ho, C.Y.; and Liley, P.E. *National Standards reference data system, Thermal conductivity of selected materials, Thermodynamic and Transport Proprieties* **1966**, U.S. department of commerce, National bureau of standards.

(20) Lee, D.W.; and Kingery, W.D. Radiation energy transfer and thermal conductivity of ceramic oxides. *J. Am. Cer. Soc.* **1960**, 43, 594.

(21) Aspnes, D. E.; Studna, A. A. Dielectric Functions and Optical Parameters of Si, Ge, GaP, GaAs, GaSb, InP, InAs, and InSb from 1.5 to 6.0 eV. *Phys. Rev. B* **1983**, 27, 985-1009.

(22) Palik, E. D. *Handbook of Optical Constants of Solids* **1985**, Academic Press, Boston.

(23) Rakić, A. D.; Aleksandra B.; Jovan D.; Elazar, M.; and Majewski, M. L. Optical properties of metallic films for vertical-cavity optoelectronic devices. *Appl. Opt.* **1998**, 37, 5271-5283.

(24) Malitson, I. H. Interspecimen comparison of the refractive index of fused silica. *J. Opt. Soc. Am.* **1965**, 55, 1205-1208.

(25) Lloyd, J. R.; Moran, W. R. Natural Convection Adjacent to Horizontal Surface of Various Planforms. *J. Heat Transf.* **1974**, 96, 443-447.

(26) Goldstein, R. J.; Sparrow, E. M.; Jones, D. C. Natural Convection Mass Transfer Adjacent to Horizontal Plates. *Int. J. of Heat and Mass Transf.* **1973**, 16, 1025-1035.

(27) Churchill, S. W.; Humbert, H.S. Correlating Equations for Laminar and Turbulent Free Convection from a Vertical Plate. *Int. J. Heat and Mass Transf.* **1975**, 18, 1323-1329.

(28) Schulenberg, T. Natural Convection Heat Transfer Below Downward Facing Horizontal Surfaces. *Int. J. Heat and Mass Transf.* **1985**, 28, 467-477.

(29) Churchill, S.W. *Heat Exchanger Design Handbook, Free Convection around Immersed Bodies* **1983**, Hemisphere Publishing, New York.

(30) Thornton, S. T.; Rex, F. A. *Modern Physics for Scientists and Engineers* **2013**, Saunders College ublishing, Boston.

(31) Chen, J.; Zhang, G.; Li, B. Thermal Contact Resistance Across Nanoscale Silicon Dioxide and Silicon Interface. *J. Appl. Phys.* **2012**, 112, 064319.

(32) Lanord, A. F.; Blandre, E.; Albaret, T.; Merabia, S.; Lacroix, D., Termentzidis, K. Atomistic Amorphous/Crystalline Interface Modelling for Superlattices and Core/Shell Nanowires. *J. Cond. Mat. Phys.* **2014**, 26, 355801.

(33) Jellison Jr, G. E.; Modine, F.A. Optical absorption of silicon between 1.6 and 4.7 eV at elevated temperatures. *Appl. Phys. Lett.* **1982**, 41, 180.

(34) Bejan, A. *Heat Transfer*, John Wiley & Sons, **1993**.

(35) Wang, M.; Yang, N.; Zeng-Yuan, G. Non-Fourier heat conductions in nanomaterials. *J. Appl. Phys.* **2011**, 110, 064310.

(36) Guo, Z. Y.; J. Motion and transfer of thermal mass-thermal mass and thermon gas. *J. Eng Thermophys.* **2006**, 27, 631.

(37)Cheng, C.; Fan, W.; Cao, J.; Ryu, S-G.;Ji, J.; Grigoropoulos, C. P.; Wu, J. Heat Transfer across the Interface between Nanoscale Solids and Gas. *ACS Nano*, **2011**, 5, 10102.

(38)Dong, Y.; Cao, B-Y.; Guo Z-Y. Generalized heat conduction laws based on thermomass theory and phonon hydrodynamics. *J. Appl. Phys.* **2011**, 110, 063504.

(39) Yu, V.; Gridneva, I. V.; Golubenko, A. A. Construction of Stress-Strain curves for brittle materials by indentation in a wide temperature range. *Sci. Sinter.* **2007**, 39, 67.